Emittance preservation under multifaceted CSR effects in isochronous deflection structures for multikiloampere bunches

Xiuji Chen, Si Chen,* Duan Gu, and Haixiao Deng†

Shanghai Advanced Research Institute, Chinese Academy of Sciences, Shanghai 201210, China

(Received 17 April 2026; accepted 28 September 2026; published 27 October 2026)

In modern accelerator facilities, coherent synchrotron radiation (CSR) presents a fundamental limitation to maintaining high-brightness electron-beam quality during deflection, with accurate modeling of its effects remaining an outstanding challenge. This study introduces a novel optimization method using an integral approach to suppress CSR-induced transverse emittance degradation under two representative bunch scenarios: ultrashort bunches and high-charge long bunches. We present analytical solutions for suppressing CSR effects in the dipoles across several quadruple-bend-achromat (QBA) layouts and establish general conditions for mitigating CSR-induced emittance growth in the subsequent drift sections of isochronous beamlines. Our analysis demonstrates that the QBA is the minimal configuration capable of simultaneously suppressing transverse emittance degradation and preserving the longitudinal beam distribution. Beam tracking results show negligible emittance growth for multikiloampere bunches at a 16° deflection. Furthermore, multicell simulation confirms the exact scalability of this approach. While previous designs suffer severe emittance degradation upon cascading, the QBA maintains exceptionally preserved beam quality.

DOI: 10.1103/78p2-pp2w

I. INTRODUCTION

Particle accelerators represent indispensable infrastructure for frontier scientific research, producing high-energy particle beams and intense radiation pulses, including x-rays [1,2] and terahertz waves [3], that interrogate matter on femtosecond to attosecond timescales. Particle accelerator applications extend from medical imaging and cancer therapy to advanced materials engineering and semiconductor lithography, establishing accelerators as cornerstone technologies driving innovation, economic growth, and societal welfare [4,5].

High-brightness electron beams, characterized by high current and low emittance, play an increasingly critical role in modern particle accelerator applications, particularly in linear colliders [6,7], plasma wakefield accelerators [8,9], and notably in x-ray free-electron lasers (XFELs) [1,10] and recirculating linacs [11–14]. In many of these systems, deflecting high-brightness beams is necessary to accommodate physical layout constraints or to enable phase-space manipulation, such as in the multibeamline operation of XFELs and the return arcs of energy-recovery linacs [15,16]. However, when such beams, especially those with ultrashort-bunch length or ultrahigh bunch charge, traverse curved trajectories, the coherent synchrotron radiation (CSR) effects in bends and in the subsequent drift sections can induce substantial energy spread and emittance growth, significantly degrading beam quality.

The suppression of CSR effects in multibend beamlines, both with and without bunch compression, has been widely investigated. In a compressor, the objective is to achieve simultaneous bunch compression and CSR suppression [17–23]. In contrast, the longitudinal profile must be preserved while mitigating CSR in noncompressing deflection lines. For otherwise comparable bunch charge, final bunch length, and total bending angle, the cumulative CSR effect can be more pronounced in an isochronous arc because the bunch remains short throughout the arc, whereas in a bunch compressor, the minimum bunch length is typically reached only near the compressor exit [21,24]. One routine strategy for isochronous beamlines is to incorporate a microbend within a double-bend achromat structure to maintain isochronicity [25–29], together with a π phase advance to enable CSR self-cancellation [25]. Another commonly employed solution is the triple-bend achromat (TBA) structure [24,30–32]. One proposed TBA structure provides theoretical compensation for the horizontal displacement induced by steady-state CSR (ss-CSR) [33]. However, its practicality is limited at large

*Contact author: chensi@sari.ac.cn
†Contact author: denghx@sari.ac.cn

Published by the American Physical Society under the terms of the Creative Commons Attribution 4.0 International license. Further distribution of this work must maintain attribution to the author(s) and the published article's title, journal citation, and DOI.

bending angles due to pronounced defocusing effects [24]. Additional limitations will be discussed in the main text.

The CSR effect on electron bunches is usually investigated by employing a 1D projected model. Based on this model, the R-matrix method and beam-envelope matching through Twiss-parameter optimization have been developed to mitigate CSR effects [34,35]. The R-matrix method was modified into the kick-point method to analyze horizontal displacements in one dipole magnet [26]. The integration method provides another approach for predicting CSR-induced emittance growth, with the optimization remaining independent of specific bunch parameters under the rigid-bunch approximation [33,36].

This paper is organized as follows. Section II extends the integral method of Ref. [33] to derive conditions for suppressing CSR effects. Section II A treats CSR in the dipoles and derives the corresponding conditions for the ss-CSR and transient CSR (tr-CSR) cases. Section II B develops an approximate model for CSR in the subsequent drift sections under the small-ϕ approximation and, based on this model, establishes general conditions for suppressing the associated CSR effects. Section III applies these conditions to symmetric isochronous quadruple-bend achromats and derives an arclike quadruple-bend-achromat (QBA) solution, satisfying the relevant bend-CSR condition together with the conditions for the subsequent drift sections. Section IV validates the analytical results through single- and multicell tracking, including the complete CSR wake and higher-order optical corrections. Section V summarizes the conclusions. Appendix A discusses the limitations of isochronous TBA cells, Appendix B presents solutions for other QBA layouts, and Appendix C collects the analytical expressions for CSR-induced emittance growth used in the simulations.

II. MITIGATION OF CSR EFFECTS

Based on the 1D projected model [37,38], the CSR effect depends solely on the natural coordinate s and the electron's longitudinal position z. Within linear single-particle dynamics, the transverse phase-space coordinates of an electron at the observation point s_f can be decomposed into three contributions: the nominal betatron motion, the dispersive contribution associated with its energy deviation, and the offsets generated by CSR-induced energy changes accumulated along the beamline. At any location s along the beamline, the CSR wake induces a local energy variation $d\delta_{\mathrm{csr}}(z,s)$ for a single particle. In a dispersive section, this local energy variation couples through the downstream transfer matrix to produce infinitesimal transverse offsets at the final position s_f. Hereafter, these CSR-induced transverse offsets are referred to as CSR kicks and are given by:

$$\begin{aligned} dx_{\mathrm{csr}}(z) &= d\delta_{\mathrm{csr}}(z,s)\cdot R_{16}^{s\to s_f}, \\ dx'_{\mathrm{csr}}(z) &= d\delta_{\mathrm{csr}}(z,s)\cdot R_{26}^{s\to s_f}, \end{aligned} \tag{1}$$

where $R_{16}^{s\to s_f}$ and $R_{26}^{s\to s_f}$ are the dispersion elements of the transfer matrix from the current position s to the exit s_f. Assuming the deflection occurs only in the horizontal plane, the total CSR-induced transverse offsets at s_f can be obtained by integrating these infinitesimal kicks along the entire beamline. Let $R^{\mathrm{rev}}(s)\equiv(R^{s\to s_f})^{-1}$ denote the transfer matrix of the reverse beamline from s_f to s. The symplectic condition then gives $R_{16}^{s\to s_f}=R_{52}^{\mathrm{rev}}(s)$ and $R_{26}^{s\to s_f}=-R_{51}^{\mathrm{rev}}(s)$. Thus, based on the integration method, the total CSR kicks x_{csr} and x'_{csr} at s_f can be expressed as:

$$\begin{aligned} x_{\mathrm{csr}}(z) &= \int_{s_f}^{s_0}\frac{d\delta_{\mathrm{csr}}(z,s)}{ds}\cdot R_{52}^{\mathrm{rev}}(s)ds, \\ x_{\mathrm{csr}}{}'(z) &= -\int_{s_f}^{s_0}\frac{d\delta_{\mathrm{csr}}(z,s)}{ds}\cdot R_{51}^{\mathrm{rev}}(s)ds. \end{aligned} \tag{2}$$

The subscripts 0 and f refer to the entrance and exit of the beamline, respectively. The quantities $R_{5i}^{\mathrm{rev}}(s)$ $(i=1,2)$ are elements of the transfer matrix of the reverse beamline and are abbreviated as R_{5i} below. The δ_{csr} is the energy spread caused by CSR, and the $\delta'_{\mathrm{csr}}(z)$ is the variance in CSR-induced energy for any s. The above expressions are derived from Eqs. (3) and (4) in Ref. [33] through a simple transformation, owing to the symplectic condition of the transfer matrix. This formulation bypasses the computational overhead of calculating the transfer matrix from every emission point to the final position $(s\to s_f)$, enabling the total CSR kicks to be evaluated directly using the reverse beamline. Accordingly, the integration in Eq. (2) proceeds from the observation point s_f back to the beamline entrance s_0.

A. CSR kicks in bends

CSR in a dipole can occur in two cases: ss-CSR and tr-CSR. A transient angle, $\theta_T=[24\sigma_z/(1.6\rho)]^{1/3}$, is introduced to distinguish these two cases [39], where σ_z is the bunch length and ρ is the dipole bending radius. Denoting the bending angle of a single dipole by θ_B, a critical bunch length σ_T is defined by the condition $\theta_T=\theta_B$.

For regions where $\theta<\theta_T$, the radiation slippage distance is significantly shorter than the bunch length. From a single-particle dynamics perspective, the instantaneous CSR wake force $W(z,s)$ is governed by the 1D Liénard–Wiechert potentials, comprising the entrance boundary terms (which subtract the upstream straight-line space-charge field) and a truncated radiation integral:

$$W(z,s)=\underbrace{\frac{4}{s}[\lambda(z-z_B)-\lambda(z-4z_B)]}_{W_{\text{bound}}}+\underbrace{\frac{2}{(3\rho^2)^{\frac{1}{3}}}\int_0^{z_B}\frac{1}{\tau^{\frac{1}{3}}}\frac{\partial\lambda(z-\tau)}{\partial z}d\tau}_{W_{\text{int}}}, \tag{3}$$

where $s=\rho\phi$ is the path length in the bend and $z_B=s^3/(24\rho^2)$ is the slippage limit from the entrance edge. In this early transient stage ($z_B\ll\sigma_z$), we can apply a first-order Taylor expansion to the delayed longitudinal density, $\lambda(z-\Delta z)\approx\lambda(z)-\Delta z\lambda'(z)$.

Under this expansion, the boundary contribution is $W_{\text{bound}}\approx(1/2)(s^2/\rho^2)\lambda'(z)$, consistent with Eq. (9) of Ref. [39]. To obtain the complete transient wake, the internal dipole radiation must also be included. Employing the zero-order approximation $\lambda'(z-\tau)\approx\lambda'(z)$ inside the integral gives:

$$W_{\text{int}}\approx\frac{2\lambda'(z)}{(3\rho^2)^{1/3}}\left(\frac{3}{2}z_B^{2/3}\right)=\frac{1}{4}\frac{s^2}{\rho^2}\lambda'(z). \tag{4}$$

Adding this integral contribution to the boundary result of Ref. [39], the total instantaneous transient wake is approximated by:

$$W_{\text{tr}}(z,s_B)\approx\frac{3}{4}\frac{s_B^2}{\rho^2}\lambda'(z), \tag{5}$$

where s_B is the local path-length coordinate measured from the entrance of each dipole. Converting the wake into the rate of change of the relative energy deviation gives:

$$\delta'_{\text{csr,tr}}(z,s_B)\approx\frac{3r_c}{4\gamma\rho^2}s_B^2\lambda'(z). \tag{6}$$

When the bunch-length variation is negligible, $\lambda'(z)$ is independent of s_B. Furthermore, the QBA cells considered below consist of identical dipoles with the same constant bending radius. Therefore, all factors in Eq. (6), except s_B^2, can be taken outside the transport integrals in Eq. (2). For a bunch satisfying $\sigma_z\geq\sigma_T$, CSR remains in the transient regime throughout each dipole. The corresponding CSR-induced transverse offsets are therefore proportional to the integrals weighted by s_B^2. Their suppression requires

$$I_{1(2)}=\int_{s_f}^{s_0}R_{51(2),B}(s)s_B^2(s)ds=0. \tag{7}$$

For a bunch satisfying $\sigma_z\ll\sigma_T$, the entrance-transient contribution becomes negligible, and the CSR wake approaches the steady-state regime [33]. The corresponding rate of change of the relative energy deviation is

$$\delta'_{\text{csr,ss}}(z)=\frac{2r_c}{3^{\frac{1}{3}}\rho^{\frac{2}{3}}\gamma}\int_{-\infty}^{z}\frac{1}{(z-z')^{\frac{1}{3}}}\frac{\partial\lambda(z',s)}{\partial z'}dz'. \tag{8}$$

When the bunch-length variation is negligible, $\delta'_{\text{csr,ss}}(z)$ is independent of the local path-length coordinate. Substitution into Eq. (2) then gives the steady-state suppression conditions:

$$I_{1(2)}=\int_{s_f}^{s_0}R_{51(2),B}(s)ds=0. \tag{9}$$

The subscripts B and D denote quantities evaluated in the dipoles and subsequent drift sections, respectively.

B. CSR kicks in the subsequent drift sections

Although most previous studies have focused on ss-CSR in the dipoles, CSR continues to affect the bunch in the subsequent drift sections. Previous analyses considered chicane compressors, in which these sections contain only drifts [20,40]. More general beamlines containing quadrupoles in the subsequent drift sections therefore require a separate treatment. Because a closed-form analytical solution is difficult to obtain, we start from Eq. (15) of Ref. [41], from which the CSR-induced energy variation in the subsequent drift sections can be written as:

$$\delta'_{\text{csr},D}=\frac{4r_c}{\gamma}\left[\frac{\lambda(z-z_D)}{\rho\theta_B+2l}+\int_{z-z_D}^{z}\frac{1}{\rho\phi+2l}\frac{\partial\lambda(z')}{\partial z'}dz'\right], \tag{10}$$

where l is the subsequent sections coordinate of the bends. Following integration by parts, variable transformation from z' to ϕ' via the Jacobian and retention of only the zeroth-order term in the ϕ expansion, the $\delta'_{\text{csr},D}$ can be approximated as:

$$\delta'_{\text{csr},D}(z)=\frac{4r_c}{\gamma}\left[\lambda(z)\int_{\phi_0}^{0}\frac{\rho}{(\rho\phi+2l)^2}d\phi-\frac{\lambda(z)}{2l}\right], \tag{11}$$

where ϕ_0 is the maximum displacement angle in the two-particle model, and its maximum value does not exceed the bend angle. Furthermore, for the case where the bunch length is much smaller than l, the ϕ_0 meets the condition as follows:

$$\sigma_z\approx\frac{\rho\phi_0^3}{24}\left(\frac{4l+\rho\phi_0}{l+\rho\phi_0}\right)\approx\frac{\rho\phi_0^3}{6}. \tag{12}$$

Based on Eq. (12), the $\delta'_{\text{csr},D}(z)$ for any z can be expressed as:

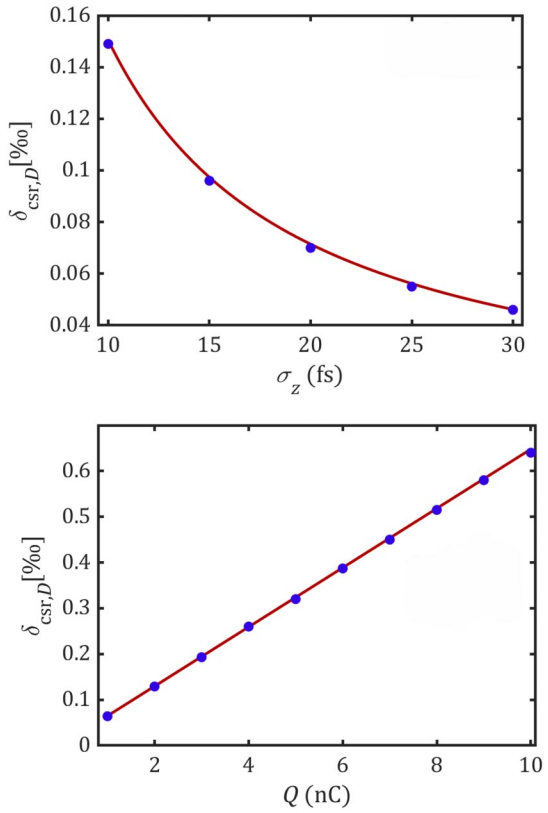


FIG. 1. Rms relative energy spread induced by CSR in the subsequent drift sections as functions of rms bunch length (top) and bunch charge (bottom). The solid curves are calculated from Eq. (14), and the markers are obtained from Bmad tracking. The bend parameters are listed in Table II, and $l = 3$ m.

$$\delta'_{\mathrm{csr},D}(z) = \frac{4r_c\lambda(z)}{\gamma(\frac{4l^2}{\rho\phi_0} + 2l)}. \tag{13}$$

For a Gaussian distribution, the rms relative energy spread induced by CSR in the subsequent drift sections is

$$\delta_{\mathrm{csr},D} = \sqrt{\frac{2\sqrt{3}-3}{3\pi}}\frac{Nr_c}{\gamma\sigma_z}\log\left(\frac{2l}{\rho\phi_0} + 1\right). \tag{14}$$

This result is analogous to Eq. (27) of Ref. [39]. Here, the numerical prefactor is obtained analytically by evaluating the rms energy spread for a Gaussian longitudinal distribution rather than by fitting tracking results. To benchmark Eq. (14) for subsequent drift sections containing focusing elements, we use the 1D CSR model in Bmad, which includes CSR transport through sections containing quadrupoles [42,43]. The Bmad tracking results shown in Fig. 1 agree closely with Eq. (14) for both the bunch-length and bunch-charge scans. In particular, the agreement is maintained for the longer bunches considered here, confirming that the small-ϕ approximation remains valid over the parameter range shown.

According to Eq. (2), after considering the CSR in the subsequent drift sections, the CSR kick of z at the exit of the beamline can be expressed as follows:

$$\begin{aligned} x_{\mathrm{csr}}(z) &= x_{\mathrm{csr},B}(z) + x_{\mathrm{csr},D}(z) \\ &= \int_{s_f}^{s_0}\frac{d\delta_{\mathrm{csr},B}}{ds}R_{52,B}\,ds + \int_{s_f}^{s_0}\frac{d\delta_{\mathrm{csr},D}}{ds}R_{52,D}\,ds, \end{aligned}$$

$$\begin{aligned} x'_{\mathrm{csr}}(z) &= x'_{\mathrm{csr},B}(z) + x'_{\mathrm{csr},D}(z) \\ &= -\int_{s_f}^{s_0}\frac{d\delta_{\mathrm{csr},B}}{ds}R_{51,B}\,ds - \int_{s_f}^{s_0}\frac{d\delta_{\mathrm{csr},D}}{ds}R_{51,D}\,ds. \end{aligned}$$

Based on the invariance of R_{5i} in nonbend regions and Eq. (13), the CSR kicks in the subsequent drift sections are

$$\begin{aligned} x_{\mathrm{csr}}(z) &= \frac{4r_c\lambda(z)}{\gamma}\sum_{i=1}^{n}R_{52,i}\omega_i, \\ x'_{\mathrm{csr}}(z) &= -\frac{4r_c\lambda(z)}{\gamma}\sum_{i=1}^{n}R_{51,i}\omega_i, \end{aligned} \tag{15}$$

where

$$\omega_i = \frac{1}{2}\ln\left(1 + \frac{2L_{D,i}}{\rho_{i+1}\phi_{0,i+1}}\right).$$

The $L_{D,i}$ is the total length between the i-th bend and the $(i+1)$-th bend of the reverse beamline. $R_{5j,i}$ is the transfer matrix for the subsequent drift of the i-th bend. It can be found that the CSR kick in the subsequent drift sections can be completely canceled for any z by requiring the sums in Eq. (15) to vanish. For any structure with negligible variance in bunch length, the following relationship must be satisfied for the reverse beamline:

$$\begin{aligned} \sum_{i=1}^{n}R_{51,i}\ln\left(1 + \frac{2L_{D,i}}{\rho_{i+1}\phi_{0,i+1}}\right) &= 0, \\ \sum_{i=1}^{n}R_{52,i}\ln\left(1 + \frac{2L_{D,i}}{\rho_{i+1}\phi_{0,i+1}}\right) &= 0. \end{aligned} \tag{16}$$

It should be noted that in the i-th term of each sum, the parameters ρ_{i+1} and $\phi_{0,i+1}$ come from the $(i+1)$-th bend of the reverse beamline.

Using the reverse beamline, we have examined CSR kicks throughout the deflection beamline. CSR in the dipoles is classified according to the ratio σ_z/σ_T. For $\sigma_z \ll \sigma_T$, the wake reaches steady state, and the corresponding suppression condition is given by Eq. (9). For $\sigma_z \geq \sigma_T$, CSR remains transient throughout each dipole; using the refined transient wake in Eq. (6), which includes both the boundary and internal-radiation contributions, the corresponding suppression condition is given by Eq. (7).

For CSR in the subsequent drift sections, an approximate analytical solution valid for general beamline configurations is derived, leading to the general conditions in Eq. (16). With these conditions established, the task is to find the simplest isochronous beamline that satisfies them simultaneously.

III. THE QBA SECTION WITH COMPLETE CSR SUPPRESSION

As discussed in Sec. II, complete cancellation of the CSR kicks requires (i) isochronicity and achromaticity and (ii) satisfaction of Eq. (9) [or Eq. (7)] together with Eq. (16). In practical applications, several additional conditions need to be satisfied, such as the performance of transverse focusing. The symmetric TBA is the simplest isochronous multibend configuration, and its limitations are analyzed in Appendix A. As follows directly from Eq. (2), I_1 and I_2 govern the CSR-induced angular and position offsets, respectively; hence, setting $I_{1(2)} = 0$ eliminates the CSR-induced offsets in both x and x' at the beamline exit. Previous studies proposed $m_{22} = -1/2$ to impose $I_1 = 0$ [24] or $m_{22} = -17/4$ to impose $I_{1(2)} = 0$ for exact CSR cancellation [33]. m_{ij} is the transfer matrix of the matching sections in the TBA cells. For $m_{22} = -\frac{1}{2}$, the reverse beamline satisfies $R_{51,1} = -R_{51,2}$ and $R_{52,1} = -\frac{1}{2}R_{52,2}$. This implies that the second condition in Eq. (16) cannot be satisfied. Meanwhile, the nonzero I_2 leaves a residual ss-CSR kick in x. When $m_{22} = -\frac{17}{4}$, the ss-CSR kicks are completely canceled on both the x and x' axes. For $m_{22} = -\frac{17}{4}$, the reverse beamline satisfies $R_{51,1} = \frac{13}{2}R_{51,2}$ and $R_{52,1} = 33R_{52,2}$. This implies that both conditions in Eq. (16) cannot be satisfied. The large values of $R_{51,2}$ and $R_{52,2}$ lead to significant CSR-induced displacements in the subsequent drift sections. Moreover, the insufficient transverse focusing makes it difficult to cascade multiple structures in practical applications. A fundamental limitation of the symmetric TBA structure is the lack of sufficient degrees of freedom to simultaneously satisfy both transverse focusing constraints and the exact CSR-cancellation conditions. To resolve this, we utilize a symmetric isochronous QBA. The addition of the fourth bend provides the exact number of free variables required to completely decouple the CSR suppression from the linear optics. By systematically varying the deflection directions of these bends, four distinct symmetric QBA configurations emerge, each tailored to specific applications. This study concentrates on the arclike QBA configuration (as illustrated in Fig. 2), while alternative bending topologies including chicane, zigzag, and dogleg geometries are analyzed in Appendix B. Under the small-angle approximation, the matching-section matrix elements of a QBA that completely suppresses ss-CSR kicks according to Eq. (9) are given by:

$$
\begin{aligned}
m_{11,1} &= \frac{1}{6}(-4 - 3\rho\theta_B m_{21,1} + g),\\
m_{12,1} &= -\frac{\rho\theta_B(6 + m_{22,1}(4 + 3\zeta))}{6\zeta},\\
m_{11,2} &= -\frac{(2 + 3\zeta)(3 + 5\zeta - m_{22,1})}{m_{22,2}(-16 + 3\zeta + g)},\\
m_{12,2} &= \frac{\rho\theta_B(2 + 3\zeta)(-8 + 15\zeta - 3m_{22,1} + \frac{1}{2}g)}{6m_{22,2}(-16 + 3\zeta + g)},\\
m_{21,2} &= -\frac{6m_{22,2}(2 + \zeta)}{\rho\theta_B(2 + 3\zeta)},\\
\zeta &= 2m_{22,1} + m_{21,1}\rho\theta_B,\\
g &= \frac{12 + 8m_{22,1}}{\zeta}.
\end{aligned}
\tag{17}
$$

The $m_{ij,1}$ is the matching section between the first and the second bends of the reverse beamline, and $m_{ij,2}$ is the matching section between the second bends and the midpoint of the reverse beamline. Note that there exists a set of solutions that simultaneously satisfies both conditions in Eq. (9) or (7), similar to case A in Appendix A. This results in three free variables instead of two, providing more degrees of freedom in the design.

The comparison in Fig. 3 demonstrates that the small-angle analytical solution agrees well with the numerical solution for bending angles below 15°. At larger angles, the local R_{56} can no longer be neglected, resulting in degraded suppression of ss-CSR kicks. For the bunches with $\sigma_z \geq \sigma_T$, to completely suppress tr-CSR kicks, the $m_{ij,k}$ are

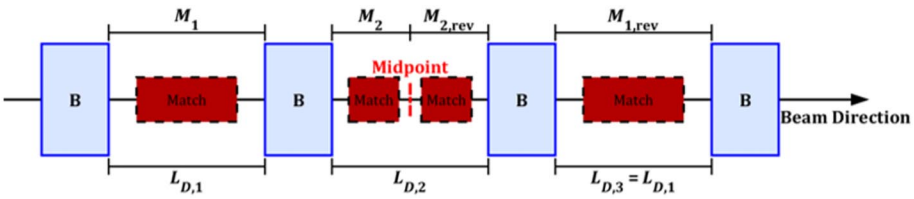


FIG. 2. Schematic of the symmetric QBA cell for exact CSR cancellation. The beam propagates along the s axis through four dipoles, with each matching section containing three quadrupole magnets for transverse focusing and optical matching. The upstream optical matrices (M_1, M_2) and drift lengths are perfectly mirrored by their reversed counterparts ($M_{2,\mathrm{rev}}$, $M_{1,\mathrm{rev}}$), with $L_{D,3} = L_{D,1}$ downstream.

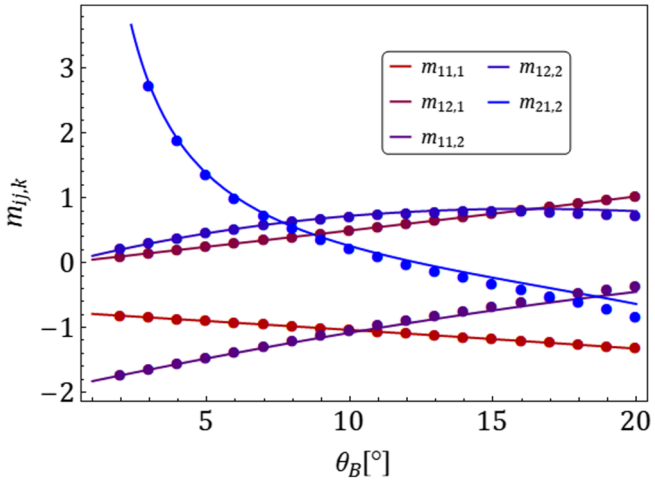


FIG. 3. Comparison between the matrix elements $m_{ij,k}$ obtained from Eq. (17) (lines) and the numerical solutions without the small-angle approximation (dots), for $\rho = 4$ m, $m_{21,1} = 0.72$, $m_{22,1} = -1.3$, and $m_{22,2} = -1.1$.

$$m_{11,2} = -\frac{(2+3\zeta)(20+33\zeta-6m_{22,1})}{2m_{22,2}(-56+9\zeta+3g)},$$
$$m_{12,2} = \frac{\rho\theta_B(2+3\zeta)(-18+33\zeta-6m_{22,1}+g)}{4m_{22,2}(-56+9\zeta+3g)}. \tag{18}$$

Other elements are identical to the QBA solution shown in Eq. (17). The analytical solutions show excellent agreement with numerical solutions (not shown). Furthermore, within a specific range of $\rho\theta_B m_{21,1}$ and $m_{22,1}$ in Fig. 4, the solutions of Eqs. (9) and (7) exhibit a deviation of less than 5%. This implies that for operating points within this range, the beamline can simultaneously mitigate CSR kicks in bends under both approximations.

There are three degrees of freedom remaining to fulfill additional constraints. For instance, $|M_{11}+M_{22}|$ can be expressed as follows:

$$|M_{11}+M_{22}| = \left|2\left(-\frac{1}{3}+g - \frac{4(49+27m_{22,1}-\frac{1}{2}g(41+3m_{22,1}))}{-48+9\zeta+3g}\right)\right|.$$

M_{ij} the transfer matrix of total beamline. An effective design approach is to adjust $|M_{11}+M_{22}|$ by modifying $m_{21,1}$ and $m_{22,1}$. Subsequently, $m_{22,2}$ is tuned to regulate the values of $m_{ij,k}$, preventing localized overfocusing or defocusing in the structure.

The conditions in Eq. (16) can be achieved by adjusting the length of the matching section. In the symmetric QBA structures, we have $L_{D,1} = L_{D,3}$. For the QBA that meets the conditions in Eq. (17), the $L_{D,2}$ meets

$$L_{D,2} = \frac{\rho\phi_0}{2}\left(\left(1+\frac{2L_{D,1}}{\rho\phi_0}\right)^{-\frac{3\zeta+g-16}{\zeta(6+\zeta)}} - 1\right). \tag{19}$$

Similar solutions for other QBA configurations can be obtained by substituting the corresponding parameters g and ζ given in Appendix B.

Moreover, for the QBA in Eqs. (17) and (18), we have $I_2 = -\frac{\rho\theta_B(6+\zeta)}{2(6+6m_{22,1}+\rho\theta_B m_{21,1})} I_1$. The emittance growth induced by CSR in the dipoles, as described by Eq. (C1) in Appendix C, therefore depends only on I_1. Thus, tuning I_1 dictates the evolution of the final emittance. To justify the ss-CSR approximation in the dipoles, the ultrashort case in Table I, with $\sigma_z = 20$ fs, is used in the simulations, while the Twiss parameters at the QBA exit are constrained to remain constant. Figure 5 presents the analytical predictions from Eq. (C1) alongside the numerical tracking results. For the case considered here, the emittance dilution becomes negligible once $|I_1| < 10^{-2}$, in agreement with the theoretical prediction. Moreover, when the CSR effect within the subsequent drift sections is evaluated independently, the analytical model presented in Eq. (C8) likewise exhibits excellent agreement with the simulation results, as depicted in Fig. 5. Given that the drift lengths $L_{D,i}$ are held constant throughout the study, the CSR-induced emittance

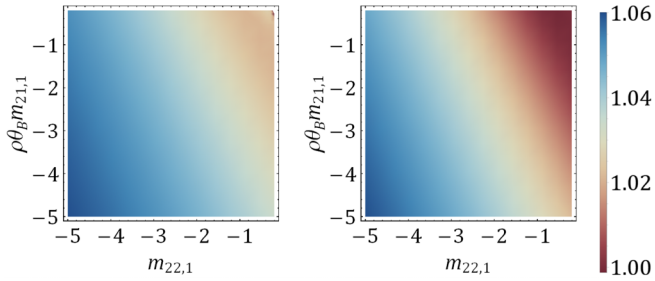


FIG. 4. Ratios of the matching-section matrix elements calculated from Eqs. (17) and (18). Left: The ratio of $m_{11,2}$ calculated using Eq. (17) to that calculated using Eq. (18). Right: The corresponding ratio for $m_{12,2}$. In each case, the common factor $1/m_{22,2}$ cancels exactly; hence, both ratios are independent of $m_{22,2}$. Ratios close to 1 identify the parameter region in which the two CSR-suppression solutions are similar.

TABLE I. Beam parameters used in the single-cell studies.

	Ultrashort case	Fixed-current scan	Unit
Bunch charge	50–300	2500–12500	pC
Rms bunch length	20	100–500	fs
Peak current	1.0–6.0	10.0	kA
Beam energy	2.0	1.0	GeV
Energy spread	0.06	0.06	%
Normalized emittance	1.00	1.00	mm mrad

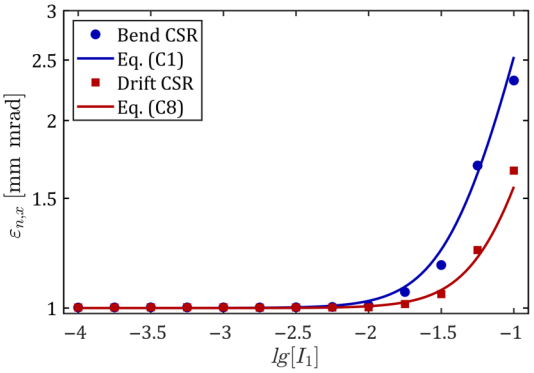


FIG. 5. Normalized horizontal emittance at the exit of the arclike QBA as a function of I_1. The beam parameters correspond to the ultrashort-bunch case with $Q = 100$ pC listed in Table I. The solid curves show the analytical predictions obtained by considering ss-CSR and CSR in the subsequent drift sections separately, and the colored markers show the corresponding Bmad simulation results.

dilution in these subsequent drift sections is also predominantly determined by I_1.

Overall, a localized parameter scan of I_1 did not yield further optimization. While the theoretical models in Eqs. (C1) and (C8) predict a slight fluctuation in emittance near $I_1 \approx 0$, this minor variation is entirely dwarfed by the significant emittance degradation resulting from the breakdown of the constant bunch-length assumption along the beamline. Concurrently, when the distinct CSR cases are evaluated independently, a substantial increase in emittance is observed, as I_1 deviates from zero. Accordingly, all subsequent simulations use the nominal QBA design specified by Eqs. (17) and (19).

IV. SIMULATIONS INCLUDING ALL CSR EFFECTS

A. CSR in a single QBA cell

Two single-cell scans are performed using the beam parameters in Table I. In the ultrashort-bunch scan, $\sigma_z = 20$ fs is fixed while the bunch charge is varied from 50 to 300 pC, corresponding to a Gaussian peak current of approximately 1–6 kA. Since $\sigma_z \ll \sigma_T$, the wake reaches the ss-CSR case within each dipole, and the QBA is configured according to the ss-CSR suppression condition.

For comparison, two previously proposed symmetric TBA beamlines are tracked under the same conditions. TBA#1 imposes $I_1 = 0$ while retaining a nonzero I_2 [24], whereas TBA#2 minimizes the Twiss-weighted emittance dilution in Eq. (C1) without requiring both integrals to vanish [44]. Neither TBA simultaneously fulfills $I_{1(2)} = 0$ and the two conditions for the subsequent drift sections in Eq. (16).

In the second scan, the Gaussian peak current is fixed at 10 kA, while σ_z is varied from 100 to 500 fs and the bunch charge changes accordingly from 2.51 to 12.53 nC. This range covers both $\sigma_z < \sigma_T$ and the pure tr-CSR case with $\sigma_z \geq \sigma_T$.

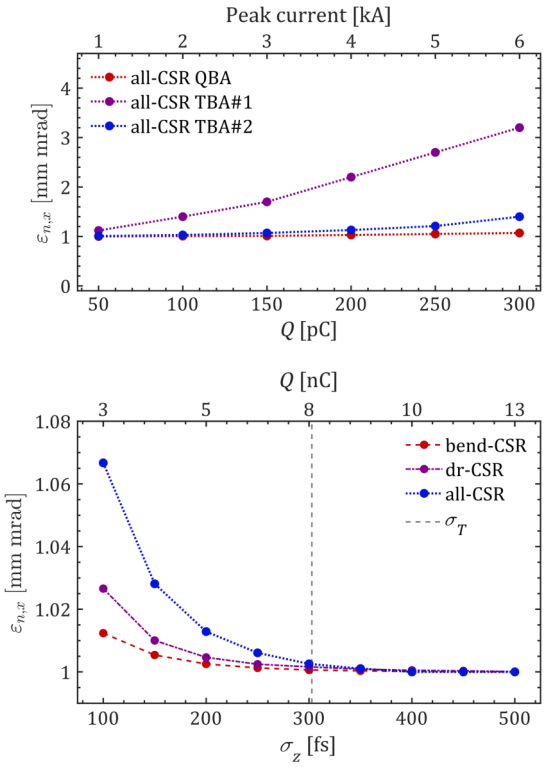


FIG. 6. Bmad-tracked normalized horizontal emittance with the dispersive contribution removed at the single-cell exits. Top: All-CSR bunch-charge scan at $\sigma_z = 20$ fs for the QBA, TBA#1, and TBA#2. Bottom: QBA bunch-length scan at a fixed Gaussian peak current of 10 kA, where bend-CSR, dr-CSR, and all-CSR denote CSR included only in the dipoles, only in the subsequent drift sections, and in both regions, respectively. The upper axes show the corresponding peak current (top) and bunch charge (bottom); the vertical dashed line marks $\sigma_T = 302.7$ fs.

The values of $L_{D,2}$ in Table II are derived from Eq. (19). The operating point is selected from the region in Fig. 4, where the values of $m_{11,2}$ and $m_{12,2}$ obtained from Eqs. (18) and (17) differ by less than 5%. All results in Fig. 6 are obtained with Bmad tracking.

TABLE II. The optimized beamline parameters of the QBA.

Parameter	Design value	Units
θ_B	4	∘
ρ	4	m
$m_{21,1}$	0.724	m^{-1}
$m_{22,1}$	−1.311	
$m_{22,2}$	−1.100	
$L_{D,1(3)}$	3.3	m
$L_{D,2}$ (ultrashort case)	2 − 2.14	m
$L_{D,2}$ (fixed-current case)	2.3	m

The upper panel of Fig. 6 shows that the QBA preserves the emittance substantially better than the two TBA beamlines, as the bunch charge increases. At $Q = 300$ pC, corresponding to a peak current of approximately 6 kA, the normalized horizontal emittances of the QBA, TBA#1, and TBA#2 are 1.070, 3.20, and 1.40 mm mrad, respectively. This difference is consistent with the suppression conditions above: residual CSR kicks remain in the two TBA beamlines, whereas the QBA satisfies $I_{1(2)} = 0$ together with Eq. (16).

For the dipole parameters in Table II, $\sigma_T = 302.7$ fs. At $\sigma_z = 100$ fs, the bend-CSR and dr-CSR cases produce emittance growths of 0.0123 mm · mrad and 0.0266 mm · mrad, respectively, whereas the all-CSR emittance growth reaches 0.0667 mm · mrad. The all-CSR emittance growth is therefore larger than that expected from a linear superposition of the bend-CSR and dr-CSR kicks obtained in the separate simulations, indicating that the rigid-bunch approximation is no longer valid when both CSR contributions are included simultaneously. The emittance growth then decreases as σ_z approaches σ_T from below. For the sampled pure tr-CSR cases with $\sigma_z \geq 350$ fs, the bend-CSR emittance remains within 0.0004 mm · mrad of its initial value, while the all-CSR emittance remains within 0.002 mm · mrad. These results confirm the effectiveness of the tr-CSR and subsequent drift suppression conditions and show that preventing the wake from reaching steady state improves single-cell emittance preservation at a fixed peak current. On the other hand, the above tracking results rely on the 1D CSR approximation, whose applicability is assessed using the Derbenev criterion $D = \sigma_x/(|\rho|\sigma_z^2)^{1/3} \ll 1$ [45], where σ_x is the local rms horizontal beam size, including the dispersive contribution. For the 20 fs case, the estimated values within the dipoles satisfy $D < 0.035$, $D < 0.131$, and $D < 0.056$ for the QBA, TBA#1, and TBA#2, respectively. Related 2D and 3D CSR studies have reported good agreement with the 1D model even for cases with larger values of D [38,46,47], which supports the use of the 1D model over the range of D considered here.

B. CSR in cascaded QBA cells

As established in Sec. III, stable periodic QBA optics allow identical cells to be cascaded for large total deflection angles. Within the first-order rigid-bunch approximation, the accumulated CSR-induced phase-space displacement after n cells is

$$\Delta\mathbf{X}_n = \sum_{k=0}^{n-1} \mathbf{M}^k \Delta\mathbf{X}_1 = (\mathbf{I} - \mathbf{M})^{-1}(\mathbf{I} - \mathbf{M}^n)\Delta\mathbf{X}_1, \quad (20)$$

where $\Delta\mathbf{X}_1 = (\Delta x, \Delta x')^T$ is the residual CSR kick at the exit of one cell, $\mathbf{M}$ is the single-cell transfer matrix, and $\mathbf{I}$ is the identity matrix. This expression requires $\mathbf{M} \neq \mathbf{I}$. Throughout this derivation, the rigid-bunch approximation is adopted, so each cell is assumed to generate the same $\Delta\mathbf{X}_1$. A small emittance variation after one cell does not necessarily imply $\Delta\mathbf{X}_1 = \mathbf{0}$, because the exit Twiss parameters can reduce the projected contribution of a residual kick. When $\Delta\mathbf{X}_1 \neq \mathbf{0}$, Eq. (20) shows that the residual kick is transported through the downstream cells and generally accumulates. By contrast, when $I_{1(2)} = 0$ and the two conditions in Eq. (16) are satisfied, the first-order residual kick vanishes, and Eq. (20) gives $\Delta\mathbf{X}_n = \mathbf{0}$ for any n.

However, Eq. (20) describes only first-order transport, which was also used in the preceding single-cell study to isolate the CSR-cancellation mechanism. Although higher-order effects are small over one cell, they can accumulate in a cascaded beamline. In particular, T_{166} and T_{266} generate energy-dependent transverse offsets that contribute to projected emittance growth, whereas T_{566} and U_{5666} distort the longitudinal phase space and local current profile [48,49].

To control accumulated higher-order aberrations, two sextupole families were introduced at mirror-symmetric locations in the QBA. The sextupole strengths were first adjusted to suppress the transverse second-order dispersion by imposing

$$T_{266,\mathrm{mid}} = 0, \quad (21)$$

where the subscript mid denotes the midpoint of the QBA cell. For a mirror-symmetric beamline structure with symmetrically arranged sextupoles and vanishing second-order dispersion at the entrance, the condition in Eq. (21) makes the second-order dispersion trajectory symmetric about the cell midpoint. Consequently, both T_{166} and T_{266} ideally return to zero at the QBA exit, consistent with a symmetry-corrected second-order achromat [50]. The third-order transverse terms U_{1666} and U_{2666} remain sufficiently small over the energy range considered and are therefore not independently optimized.

For the multicell analysis, the cell numbers were chosen to give the three beamlines comparable total deflection angles and lengths. TBA#1 and TBA#2 comprise 15 and 12 cells, respectively, and each provides a total deflection of 180°, whereas the 12-cell QBA provides 192°. Their corresponding beamline lengths are approximately 149.5, 143.7, and 136.5 m.

After imposing the midpoint constraint on T_{266}, the remaining sextupole degree of freedom was used to adjust the longitudinal second-order dispersion. To preserve the first-order conditions in Eq. (17), the first-order optics were kept unchanged while the single-cell T_{566} was scanned under the constraint $T_{266,\mathrm{mid}} = 0$. The nonlinear-optics optimization was performed with Bmad while retaining all CSR effects in the tracking. The beam parameters in Table III lie within the typical range for compressed ERL bunches [16,19]. A preliminary coarse scan over a broader range of the single-cell T_{566} (not

TABLE III. Representative parameters of a compressed bunch in an energy-recovery linac (ERL).

Parameter	Value	Unit
Bunch charge	100	pC
Rms bunch length	40	fs
Peak current	1.0	kA
Beam energy	1000	MeV
Rms relative energy spread	0.06	%
Normalized emittance	1.00	mm mrad

shown) was first performed to identify the refined range presented in Fig. 7. Within this range, the exit rms bunch length varies from 38.86 to 41.44 fs, corresponding to a maximum deviation of approximately 3.6% from the nominal value of 40 fs, whereas the peak current varies from 0.973 to 1.519 kA, a span equal to approximately 55% of its nominal value. Because nonlinear longitudinal transport has a much stronger influence on the local current profile than on the overall rms bunch length, preservation of the peak current was adopted as the primary criterion for selecting the working point at $T_{566} = 3.0 \times 10^{-3}$ m.

After the working point was selected, multicell tracking was performed using the parameters in Table III. The two cascaded TBA beamlines were not subjected to dedicated higher-order optimization. Retaining their uncompensated higher-order transverse and longitudinal dispersion would introduce additional nonlinear aberrations and longitudinal density modulation, thereby obscuring the comparison of their first-order CSR-cancellation performance. To provide a controlled comparison, first-order tracking of TBA#1, TBA#2, and the QBA was performed with Elegant [51],

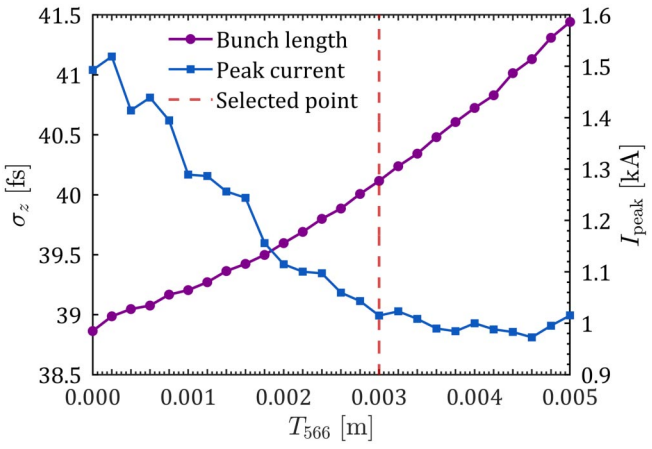


FIG. 7. Exit rms bunch length (left axis) and peak current (right axis) as functions of the single-cell T_{566} for the 12-cell cascaded QBA. The constraint $T_{266,\mathrm{mid}} = 0$ is maintained, and the peak current is estimated by averaging the three largest values in each longitudinal histogram. The vertical dashed line marks the selected working point at $T_{566} = 3.0 \times 10^{-3}$ m.

with CSR in both the dipoles and subsequent drift sections included. The QBA was then tracked in Bmad with the corrected third-order optics.

Figure 8 summarizes the beamline optics and the resulting beam evolution. The left panel presents the ideal linear-optics evolution along the cascaded QBA. The periodic behavior of the β functions and horizontal dispersion illustrates the matched transverse optics used in the multicell tracking.

The middle panel compares the normalized horizontal emittance with dispersive contributions removed. At the beamline exits, the absolute emittance growths are approximately 4.596, 2.072, and 0.0056 mm · mrad for TBA#1, TBA#2, and the first-order QBA, respectively. The much larger increases in the two TBA beamlines are consistent with Eq. (20): the residual single-cell CSR kicks identified in the previous subsection are transported through the downstream cells and accumulate. CSR in the subsequent drift sections, which is not fully suppressed in either TBA beamline, provides an additional cumulative contribution. In contrast, the 0.0056 mm · rad QBA result confirms that its first-order CSR-cancellation conditions remain effective after cascading. With the corrected third-order optics included, the QBA emittance growth increases to approximately 0.0443 mm · rad, which is 0.0387 mm· rad above the first-order result. The remaining increase arises because the sextupole optimization constrains only selected higher-order dispersion terms and does not explicitly minimize the local coupling between higher-order dispersion and CSR-induced energy deviations along the beamline. Consequently, the higher-order components of the CSR kicks are not fully canceled.

The right panel compares the exit current profile and normalized horizontal slice emittance obtained with the first- and third-order QBA models. At the selected working point, the two current profiles remain similar, and no pronounced current spike is generated by the higher-order longitudinal transport. The exit rms bunch lengths are 39.970 and 40.034 fs, corresponding to deviations of approximately 0.07% and 0.09%, respectively, from the nominal value of 40 fs. The corresponding peak currents extracted from the current profiles are 1.021 and 1.063 kA, representing variations of approximately 2.1% and 6.3% from the nominal value of 1.0 kA. These results indicate that the higher-order longitudinal effects are effectively controlled at the selected working point. The normalized horizontal slice emittance remains close to its initial value of 1 mm · mrad throughout the high-current core. Its preservation indicates that the modest increase in projected emittance after including third-order optics arises primarily from residual correlations between slices rather than substantial degradation within individual slices. Overall, the selected working point limits nonlinear longitudinal-profile distortion while preserving the transverse slice quality; furthermore, compared with compressor beamlines having

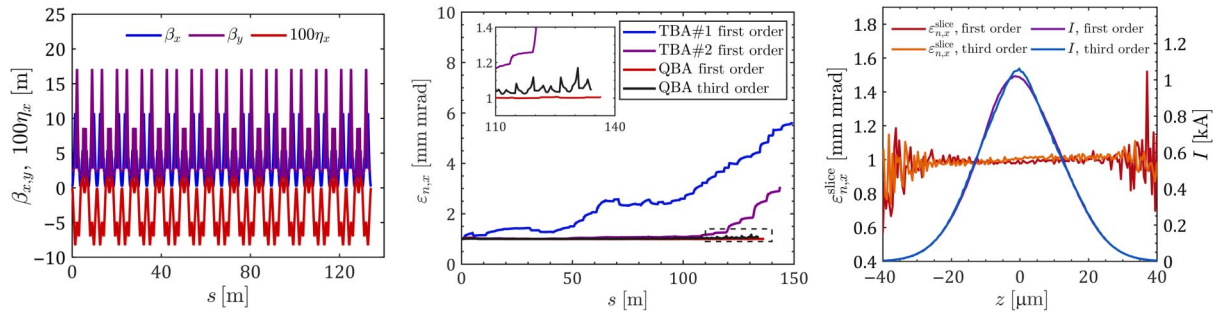


FIG. 8. Optical and beam evolution for the bunch in Table III. (Left) Horizontal and vertical β functions and the scaled horizontal dispersion $100\eta_x$ along the cascaded QBA. (Middle) Normalized horizontal emittance with the dispersive contribution removed for TBA#1, TBA#2, and the QBA. The first-order results are obtained with Elegant, whereas the corrected third-order QBA result is obtained with Bmad. The inset magnifies the QBA exit region. (Right) Normalized horizontal slice emittance (left axis) and current profile (right axis) at the QBA exit, comparing the first-order Elegant result with the third-order Bmad result. CSR in the dipoles and subsequent drift sections is included throughout.

comparable total deflection angles and final bunch parameters [17–19], the QBA exhibits low emittance growth despite the accumulation of CSR effects over multiple cascaded cells [52].

V. CONCLUSION

In summary, we have extended the first-order integral method to derive conditions for suppressing CSR-induced transverse kicks in isochronous deflection beamlines. Separate suppression conditions for CSR in bends are derived for the ss-CSR-dominated case, $\sigma_z \ll \sigma_T$, and the pure tr-CSR case, $\sigma_z \geq \sigma_T$, together with general conditions for suppressing CSR in the subsequent drift sections. Within the adopted symmetric isochronous model, the QBA is identified as the minimal multibend configuration providing sufficient degrees of freedom to satisfy these conditions while maintaining stable periodic optics. The QBA solutions obtained for the ss-CSR and tr-CSR cases remain close over a broad range of optical parameters. Therefore, the same QBA structure can be applied in either limiting case, with the corresponding suppression condition for CSR in bends imposed separately.

Single-cell tracking with all CSR effects included confirms the effectiveness of these conditions. In the ultrashort-bunch-charge scan, the QBA exhibits substantially smaller emittance growth than the two reference TBA beamlines. In the fixed-10 kA scan, the emittance growth decreases as σ_z approaches σ_T and remains negligible for the sampled pure tr-CSR cases with $\sigma_z > \sigma_T$. These results demonstrate that preventing the wake from reaching steady state can substantially improve single-cell emittance preservation at a fixed peak current.

Multicell tracking further demonstrates the scalability of the QBA suppression conditions over large total deflection angles. With first-order transport, the normalized horizontal emittance increases by approximately 4.596, 2.072, and 0.0056 mm · mrad for TBA#1, TBA#2, and the QBA, respectively. After the corrected third-order optics are included, the QBA emittance growth remains limited to approximately 0.0443 mm · mrad. At the selected sextupole working point, the rms bunch length remains within 0.1% of its nominal value, the peak-current variation remains below 6.4%, and the normalized horizontal slice emittance is preserved throughout the high-current core.

Although the present results demonstrate effective CSR suppression, their applicability is limited to the range of validity of the 1D CSR model. For even shorter or strongly chirped bunches, local compression, dispersion-induced transverse expansion, and bunch tilt can weaken this approximation, making multidimensional CSR corrections significant [38,53]. The robustness of the present CSR-suppression conditions under these more extreme beam conditions therefore requires further assessment with 2D or 3D CSR models. In addition, future work will consider profile-dependent coupling in cases where tr-CSR and ss-CSR coexist, practical magnet constraints, and additional collective effects such as longitudinal space charge.

ACKNOWLEDGMENTS

This work was supported by the National Natural Science Foundation of China (12541503, 12125508, 12241501, 12205356), the Shanghai Action Plan for Science, Technology and Innovation (No. 24JD1402800), and the Shanghai Pilot Program for Basic Research—Chinese Academy of Sciences, Shanghai Branch (JCYJ-SHFY-2021-010).

DATA AVAILABILITY

The lattice and setup files in Bmad and Elegant formats used in this study are openly available in the GitHub repository [54].

APPENDIX A: ANALYTICAL SOLUTION FOR ISOCHRONOUS TBA CELLS WITH COMPLETE SUPPRESSION OF SS-CSR EFFECTS

For a symmetric TBA composed of three identical dipoles, no solution can simultaneously satisfy all the conditions required for complete ss-CSR-kick suppression because the number of constraints exceeds the available degrees of freedom. We therefore introduce an additional degree of freedom through the ratio k between the bending angles of the middle and side dipoles, while assuming that all dipoles have the same bending radius. Under the small-angle approximation, I_1 and I_2 for a symmetric TBA cell are given by:

$$\frac{36I_1k^2}{\theta_1^2\rho} = (k+2m_{22})(28k+12k^2+8k^4+3k^5+8m_{22}+4k^3m_{22}), \tag{A1}$$

$$\frac{36I_2k^2}{\theta_1^3\rho^2} = (k+m_{22})(28k+12k^2+8k^4+3k^5+8m_{22}+4k^3m_{22}). \tag{A2}$$

θ_1 is the angle of the side bends of symmetric TBA cells. k is the ratio between the middle bend and the side bends. m_{ij} are the elements of the transfer matrix from the first bend to the second bend. To ensure that either I_1 or I_2 equals zero, the value of m_{22} must satisfy the following conditions:

$$I_1 = 0 \rightarrow \begin{cases} m_{22} = -\frac{k}{2} \\ m_{22} = -\frac{28k+12k^2+8k^4+3k^5}{4(2+k^3)}. \end{cases} \tag{A3}$$

$$I_2 = 0 \rightarrow \begin{cases} m_{22} = -k \\ m_{22} = -\frac{28k+12k^2+8k^4+3k^5}{4(2+k^3)}. \end{cases} \tag{A4}$$

The second conditions in Eqs. (A3) and (A4) are identical. Therefore, both I_1 and I_2 will equal zero when m_{22} meets this specific condition. This solution has been extensively discussed when $k = 1$ in Ref. [33]. However, TBA cells satisfying this condition exhibit excessive defocusing in the x plane, preventing them from being cascaded to achieve large deflection angles. As shown in Fig. 9, reducing k mitigates the excessive defocusing of the TBA cell; however, $M_{11}+M_{22}$ remains substantially greater than 2. It seems impossible to obtain a periodic solution for the TBA in this case by varying the value of k. We therefore consider the remaining solutions in Eqs. (A3) and (A4). Although these solutions cannot make CSR kicks simultaneously zero in both the x and x' directions, the growth in emittance caused by ss-CSR can be suppressed completely according to Eq. (C1). The values of $M_{11}+M_{22}$ for these respective cases are 2 ($m_{22} = -k$) and -2 ($m_{22} = -k/2$). Although there are no periodic solutions for the beamline in these specific cases, the asymptotic solution in the vicinity of these scenarios presents a viable solution approach. Related work can be found in Ref. [24].

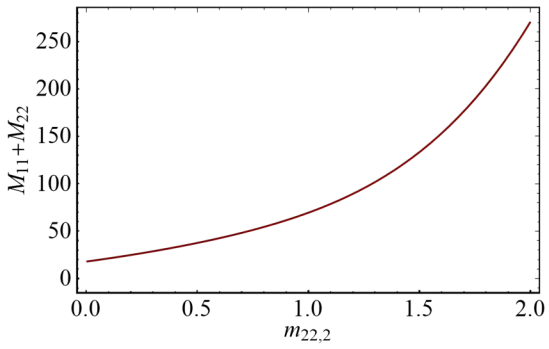


FIG. 9. The transverse focusing parameter $M_{11}+M_{22}$ as a function of k, with a singularity at $k = 0$.

The asymmetric TBA with three identical bends was considered. The elements of the transfer matrices for the matching sections between the first and second bends of the reverse beamline were represented as $m_{ij,1}$. The second matching sections of the reverse beamline were denoted as $m_{ij,2}$. M denotes the transfer matrix of the complete TBA cell. There are six degrees of freedom and six constraints for the asymmetric TBA cells. The conditions derived above yield two sets of solutions:

Case A:

$$\begin{aligned}
m_{11,1} &= -5\left(5+2\sqrt{8-m_{22,2}}\right)+m_{22,2} \\
m_{12,1} &= \frac{1}{2}L_B\left(27+11\sqrt{8-m_{22,2}}-m_{22,2}\right) \\
m_{21,1} &= \frac{66+22\sqrt{8-m_{22,2}}-2m_{22,2}}{L_B} \\
m_{22,1} &= -12\left(3+\sqrt{8-m_{22,2}}\right)+m_{22,2} \\
m_{11,2} &= -1+2\sqrt{8-m_{22,2}}+m_{22,2} \\
m_{12,2} &= -\frac{1}{2}L_B\left(3+\sqrt{8-m_{22,2}}+m_{22,2}\right) \\
m_{21,2} &= \frac{2\left(-3+\sqrt{8-m_{22,2}}+m_{22,2}\right)}{L_B}.
\end{aligned} \tag{A5}$$

Case B:

$$
\begin{aligned}
m_{11,1} &= -5(5-2\sqrt{8-m_{22,2}})+m_{22,2}\\
m_{12,1} &= \frac{1}{2}L_B(27-11\sqrt{8-m_{22,2}}+m_{22,2})\\
m_{21,1} &= \frac{66-22\sqrt{8-m_{22,2}}-2m_{22,2}}{L_B}\\
m_{22,1} &= 12(-3+\sqrt{8-m_{22,2}})+m_{22,2}\\
m_{11,2} &= -1-2\sqrt{8-m_{22,2}}+m_{22,2}\\
m_{12,2} &= -\frac{1}{2}L_B(3-\sqrt{8-m_{22,2}}+m_{22,2})\\
m_{21,2} &= \frac{2(3+\sqrt{8-m_{22,2}}-m_{22,2})}{L_B}.
\end{aligned}
\tag{A6}
$$

L_B was the total length of the bends. Then the L_B was set to 0.35 m (the angle of the bends: 5°, the radii: 4 m). Furthermore, the $M_{11}+M_{22}$ of the two TBA cases can be altered by adjusting the dimensionless quantity $m_{22,2}$. The range of $m_{22,2}$ is restricted to $-5 \le m_{22,2} \le 5$ to avoid excessive focusing or defocusing. The relationship between $M_{11}+M_{22}$ and $m_{22,2}$ is shown in Fig. 10. There are no periodic solutions for the TBA of case B within the specified range. Additionally, the defocusing is more severe than that predicted by the analytical

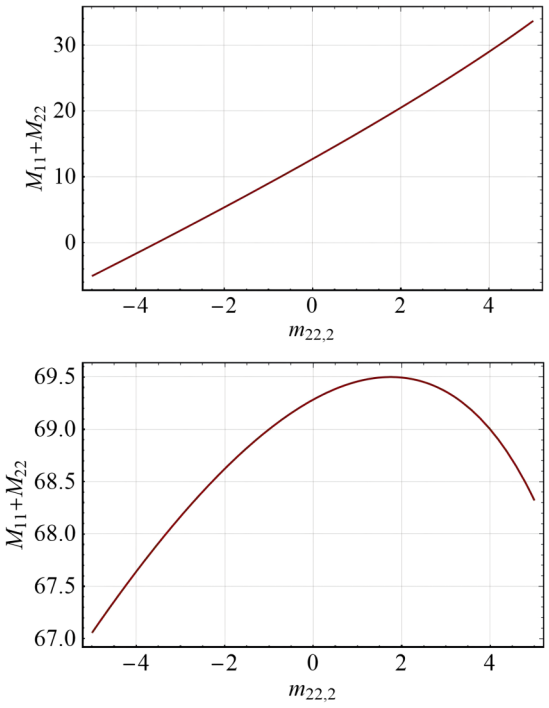


FIG. 10. The relationship between $M_{11}+M_{22}$ and $m_{22,2}$. (Top) the case A; (bottom) the case B.

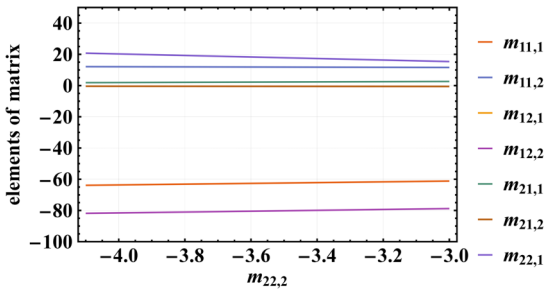


FIG. 11. Transfer-matrix elements of the two matching sections for the case-A asymmetric TBA solution in Eq. (A5), plotted as functions of the free parameter $m_{22,2}$ over the periodic-solution range $-4.1 \le m_{22,2} \le -3$, with $L_B = 0.35$ m. The large absolute values of the elements indicate strong local focusing or defocusing within this range.

symmetric TBA solution. For case A, periodic TBA solutions exist for $-4.1 \le m_{22,2} \le -3$. However, as shown in Fig. 11, the remaining matching-section matrix elements have large absolute values throughout this range. This could lead to additional beam loss. Therefore, asymmetric isochronous TBA cells with identical bends do not provide a practical solution for complete cancellation of ss-CSR kicks.

APPENDIX B: SOLUTIONS FOR FOUR QBA STRUCTURES WITH COMPLETE SUPPRESSION OF CSR KICKS IN BENDS

In this section, we present four QBA configurations that can completely suppress both ss-CSR and tr-CSR kicks. As in the arclike QBA discussed in the main text, only two elements, $m_{11,2}$ and $m_{12,2}$, differ between the solutions of Eqs. (9) and (7).

The matching-section matrices for the four isochronous QBA structures that completely suppress ss-CSR kicks are given below, where $\zeta = 2m_{22,1}+m_{21,1}L_B$:

Arclike type:

$$
\begin{aligned}
m_{11,1} &= \frac{1}{6}(-4-3L_B m_{21,1}+g_a),\\
m_{12,1} &= -\frac{L_B(6+m_{22,1}(4+3\zeta))}{6\zeta},\\
m_{11,2} &= -\frac{(2+3\zeta)(3+5\zeta-m_{22,1})}{m_{22,2}(-16+3\zeta+g_a)},\\
m_{12,2} &= \frac{L_B(2+3\zeta)(-8+15\zeta-3m_{22,1}+\frac{1}{2}g_a)}{6m_{22,2}(-16+3\zeta+g_a)},\\
m_{21,2} &= -\frac{6m_{22,2}(2+\zeta)}{L_B(2+3\zeta)},\\
g_a &= \frac{12+8m_{22,1}}{\zeta}.
\end{aligned}
\tag{B1}
$$

Chicane type:

$$
\begin{aligned}
m_{11,1} &= \frac{1}{6\zeta}(12 + L_B m_{21,1}(4 - 3\zeta)),\\
m_{12,1} &= \frac{L_B(6 + m_{22,1}(3\zeta - 4))}{6\zeta},\\
m_{11,2} &= -\frac{(3\zeta - 2)(5\zeta - m_{22,1} - 3)}{m_{22,2}(16 + 3\zeta + g_c)},\\
m_{12,2} &= \frac{L_B(3\zeta - 2)(8 + 15\zeta - 3m_{22,1} + \frac{1}{2}g_c)}{6m_{22,2}(16 + 3\zeta + g_c)},\\
m_{21,2} &= -\frac{6m_{22,2}(\zeta - 2)}{L_B(3\zeta - 2)},\\
g_c &= \frac{12 - 8m_{22,1}}{\zeta}.
\end{aligned}
\tag{B2}
$$

Zigzag type:

$$
\begin{aligned}
m_{11,1} &= \frac{1}{6\zeta}(12 + L_B m_{21,1}(4 - 3\zeta)),\\
m_{12,1} &= -\frac{L_B(6 + m_{22,1}(3\zeta - 4))}{6\zeta},\\
m_{11,2} &= -\frac{(\zeta - 2)(8 - 3m_{22,1} + 15\zeta + \frac{g_z}{2})}{m_{22,2}(16 + 3\zeta + g_z)},\\
m_{12,2} &= \frac{L_B(3\zeta - 2)(8 - 3m_{22,1} + 15\zeta + \frac{g_z}{2})}{6m_{22,2}(16 + 3\zeta + g_z)},\\
m_{21,2} &= -\frac{6m_{22,2}\zeta(5\zeta - m_{22,1} - 3)}{L_B(8 - 3m_{22,1} + 15\zeta + \frac{g_z}{2})},\\
g_z &= \frac{12 - 8m_{22,1}}{\zeta}.
\end{aligned}
\tag{B3}
$$

Dogleg type:

$$
\begin{aligned}
m_{11,1} &= \frac{1}{6}(-4 - 3L_B m_{21,1} + g_d),\\
m_{12,1} &= -\frac{L_B(6 + m_{22,1}(4 + 3\zeta))}{6\zeta},\\
m_{11,2} &= -\frac{(2 + 3\zeta)(3 + 5\zeta - m_{22,1})}{m_{22,2}(-16 + 3\zeta + g_d)},\\
m_{12,2} &= \frac{L_B(2 + 3\zeta)(-8 + 15\zeta - 3m_{22,1} + \frac{1}{2}g_d)}{6m_{22,2}(-16 + 3\zeta + g_d)},\\
m_{21,2} &= -\frac{6m_{22,2}\zeta(5\zeta + 3 - m_{22,1})}{L_B(15\zeta - 8 - 3m_{22,1} + \frac{g_d}{2})},\\
g_d &= \frac{12 + 8m_{22,1}}{\zeta}.
\end{aligned}
\tag{B4}
$$

The corresponding matching-section elements for complete suppression of tr-CSR kicks are given below:

Arclike type:

$$
\begin{aligned}
m_{11,2} &= -\frac{(2 + 3\zeta)(20 + 33\zeta - 6m_{22,1})}{2m_{22,2}(-56 + 9\zeta + 3g_a)},\\
m_{12,2} &= \frac{L_B(2 + 3\zeta)(-18 + 33\zeta - 6m_{22,1} + g_a)}{4m_{22,2}(-56 + 9\zeta + 3g_a)}.
\end{aligned}
\tag{B5}
$$

Chicane type:

$$
\begin{aligned}
m_{11,2} &= \frac{\zeta(3\zeta - 2)(33\zeta - 6m_{22,1} - 20)}{2m_{22,2}(56 + 9\zeta + 3g_c)},\\
m_{12,2} &= \frac{L_B(3\zeta - 2)(33\zeta - 6m_{22,1} + 18 + g_c)}{4m_{22,2}(56 + 9\zeta + 3g_c)}.
\end{aligned}
\tag{B6}
$$

Zigzag type:

$$
\begin{aligned}
m_{11,2} &= \frac{3(3\zeta - 2)(33\zeta - 6m_{22,1} + 18 + g_z)}{2m_{22,2}(56 + 9\zeta + 3g_z)},\\
m_{12,2} &= \frac{L_B(3\zeta - 2)(33\zeta - 6m_{22,1} + 18 + g_z)}{4m_{22,2}(56 + 9\zeta + 3g_z)}.
\end{aligned}
\tag{B7}
$$

Dogleg type:

$$
\begin{aligned}
m_{11,2} &= \frac{3(3\zeta + 2)(33\zeta - 6m_{22,1} - 18 + g_d)}{2m_{22,2}(-56 + 9\zeta + 3g_d)},\\
m_{12,2} &= \frac{L_B(3\zeta + 2)(33\zeta - 6m_{22,1} - 18 + g_d)}{4m_{22,2}(-56 + 9\zeta + 3g_d)}.
\end{aligned}
\tag{B8}
$$

For each QBA topology, a parameter range exists in which the ss-CSR and tr-CSR suppression solutions are similar, analogous to that shown for the arclike QBA in Fig. 4.

APPENDIX C: ANALYSIS OF EMITTANCE GROWTH INDUCED BY CSR KICKS IN THE SUBSEQUENT DRIFT SECTIONS

When only CSR in the bends is considered, and the entrance and exit Twiss parameters are matched to the periodic solution, the horizontal emittance at the beamline exit can be expressed as [33]:

$$
\epsilon_x^2 = \epsilon_{x0}^2 + \epsilon_{x0}(\beta_x I_1^2 + \gamma_x I_2^2 + 2\alpha_x I_1 I_2) I_{\mathrm{csr}}^2. \tag{C1}
$$

Here, ϵ_{x_0} and ϵ_x are the geometric emittances at the entrance and exit of the beamline, respectively; β_x, α_x, and γ_x are the horizontal Twiss parameters; and I_{csr} is the rms energy spread caused by ss-CSR or tr-CSR.

Furthermore, CSR in the subsequent drift sections was taken into consideration. The additional energy spread in this case is related to s, as shown in Eqs. (13)–(15). The rms of the CSR kick cannot be expressed in the simplified form presented in Eqs. (8)–(10) of Ref. [33]. It is also challenging to solve the coupling of CSR kicks

analytically in the two cases. In this study, we focus solely on QBA cases that satisfy the conditions in Eq. (17). As a result, the rms of the ss-CSR kick is close to zero, and the coupling between the two types of CSR kicks is negligible. The variance of the CSR kick in the x direction can therefore be expressed as:

$$\langle (x-\langle x\rangle)^2\rangle = \langle ((x_1-\langle x_1\rangle)+(x_2-\langle x_2\rangle)+(x_3-\langle x_3\rangle))^2\rangle$$
$$x_i = \frac{4r_c\lambda(z)R_{52,i}\omega_i}{\gamma}, \quad x_i' = -\frac{4r_c\lambda(z)R_{51,i}\omega_i}{\gamma}. \tag{C2}$$

The kick variances in the other directions follow analogous expressions. Then for any z of the bunch, the CSR kicks satisfy

$$\frac{x_i(z)}{x_j(z)} = \frac{R_{52,i}\omega_i}{R_{52,j}\omega_j}, \quad \frac{x_i(z)}{x_j'(z)} = -\frac{R_{52,i}\omega_i}{R_{51,j}\omega_j}. \tag{C3}$$

Because all $x_i(z)$ and $x_i'(z)$ are proportional to the same longitudinal function $\lambda(z)$, the absolute value of each pairwise correlation coefficient is unity, while its sign is determined by the corresponding kick coefficients. Defining $\tilde{x}_i = x_i - \langle x_i\rangle$, $\tilde{x}_i' = x_i' - \langle x_i'\rangle$, $C_i = R_{52,i}\omega_i$, and $C_i' = -R_{51,i}\omega_i$, the covariance terms satisfy

$$\langle \tilde{x}_i\tilde{x}_j\rangle = \mathrm{sgn}(C_iC_j)\sqrt{\langle \tilde{x}_i^2\rangle\langle \tilde{x}_j^2\rangle},$$
$$\langle \tilde{x}_i\tilde{x}_j'\rangle = \mathrm{sgn}(C_iC_j')\sqrt{\langle \tilde{x}_i^2\rangle\langle \tilde{x}_j'^2\rangle}. \tag{C4}$$

The corresponding variances and covariance of the CSR kicks in the subsequent drift sections are

$$\langle (x-\langle x\rangle)^2\rangle = \left(\sqrt{\frac{2\sqrt{3}-3}{3\pi}}\frac{Nr_c}{\gamma\sigma_z}\right)^2 \sum_{i,j} R_{52,i}R_{52,j}\omega_i\omega_j, \tag{C5}$$

$$\langle (x'-\langle x'\rangle)^2\rangle = \left(\sqrt{\frac{2\sqrt{3}-3}{3\pi}}\frac{Nr_c}{\gamma\sigma_z}\right)^2 \sum_{i,j} R_{51,i}R_{51,j}\omega_i\omega_j, \tag{C6}$$

$$\langle (x-\langle x\rangle)(x'-\langle x'\rangle)\rangle = -\left(\sqrt{\frac{2\sqrt{3}-3}{3\pi}}\frac{Nr_c}{\gamma\sigma_z}\right)^2 \times \sum_{i,j} R_{52,i}R_{51,j}\omega_i\omega_j. \tag{C7}$$

For the symmetric QBA considered here, the cell boundary is chosen at a symmetry point of the periodic beta function, so that $\alpha_x = 0$. At this point, $\beta_x = \sqrt{M_{12}^2/(1-M_{11}^2)}$ and $\gamma_x = \sqrt{(1-M_{11}^2)/M_{12}^2}$. Consequently, the covariance term in Eq. (C7) does not contribute to the projected emittance. After including CSR in the subsequent drift sections, the emittance at the beamline exit is therefore,

$$\epsilon_x^2 = \epsilon_{x0}^2 + \epsilon_{x0}\left(\sqrt{\frac{2\sqrt{3}-3}{3\pi}}\frac{Nr_c}{\gamma\sigma_z}\right)^2 \left(\sqrt{\frac{M_{12}^2}{1-M_{11}^2}}\sum_{i,j} R_{51,i}R_{51,j}\omega_i\omega_j + \sqrt{\frac{1-M_{11}^2}{M_{12}^2}}\sum_{i,j} R_{52,i}R_{52,j}\omega_i\omega_j\right). \tag{C8}$$

[1] P. Emma, R. Akre, J. Arthur, R. Bionta, C. Bostedt, J. Bozek, A. Brachmann, P. Bucksbaum, R. Coffee, F.-J. Decker *et al.*, First lasing and operation of an ångstrom-wavelength free-electron laser, Nat. Photonics **4**, 641 (2010).

[2] C. Pellegrini, A. Marinelli, and S. Reiche, The physics of x-ray free-electron lasers, Rev. Mod. Phys. **88**, 015006 (2016).

[3] S. Huang, Y. Ding, Y. Feng, E. Hemsing, Z. Huang, J. Krzywinski, A. A. Lutman, A. Marinelli, T. J. Maxwell, and D. Zhu, Generating single-spike hard X-ray pulses with nonlinear bunch compression in free-electron lasers, Phys. Rev. Lett. **119**, 154801 (2017).

[4] M. Goldstein, S. H. Lee, Y. A. Shroff, P. J. Silverman, D. Williams, H. Park, M. A. Piestrup, and R. H. Pantell, FEL applications in EUV lithography, in *Proceedings of the 27th International Free Electron Laser Conference (FEL'05)* (JACoW, Palo Alto, CA, USA, 2005), pp. 422–425.

[5] J. S. Loeffler and M. Durante, Charged particle therapy—optimization, challenges and future directions, Nat. Rev. Clin. Oncol. **10**, 411 (2013).

[6] F. Stulle, A. Adelmann, and M. Pedrozzi, Designing a bunch compressor chicane for a multi-TeV linear collider, Phys. Rev. ST Accel. Beams **10**, 031001 (2007).

[7] J. Wu, G. V. Stupakov, T. O. Raubenheimer, and Z. Huang, Impact of the wiggler coherent synchrotron radiation impedance on the beam instability and damping ring optimization, Phys. Rev. ST Accel. Beams **6**, 104404 (2003).

[8] E. Esarey, C. B. Schroeder, and W. P. Leemans, Physics of laser-driven plasma-based electron accelerators, Rev. Mod. Phys. **81**, 1229 (2009).

[9] C. A. Lindstrøm, Staging of plasma-wakefield accelerators, Phys. Rev. Accel. Beams **24**, 014801 (2021).

[10] N. Huang, H. Deng, B. Liu, D. Wang, and Z. Zhao, Features and futures of X-ray free-electron lasers, The Innovation **2**, 100097 (2021).

[11] P. H. Williams, D. Angal-Kalinin, D. J. Dunning, J. K. Jones, and N. R. Thompson, Recirculating linac free-electron laser driver, Phys. Rev. ST Accel. Beams **14**, 050704 (2011).

[12] A. Bartnik, N. Banerjee, D. Burke, J. Crittenden, K. Deitrick, J. Dobbins, C. Gulliford, G. H. Hoffstaetter, Y. Li, W. Lou *et al.*, CBETA: First multipass superconducting linear accelerator with energy recovery, Phys. Rev. Lett. **125**, 044803 (2020).

[13] G. Wang, J. Yan, N. Huang, D. Gu, M. Zhang, H. Deng, B. Liu, D. Wang, X. Yang, and Z. Zhao, Energy recovery operation for continuous-wave X-ray free-electron lasers, Nucl. Instrum. Methods Phys. Res. Sect. A **1005**, 165410 (2021).

[14] Z. T. Zhao, Z. Wang, C. Feng, S. Chen, and L. Cao, Energy recovery linac based fully coherent light source, Sci. Rep. **11**, 23875 (2021).

[15] T. Hara, K. Fukami, T. Inagaki, H. Kawaguchi, R. Kinjo, C. Kondo, Y. Otake, Y. Tajiri, H. Takebe, K. Togawa *et al.*, Pulse-by-pulse multi-beam-line operation for x-ray free-electron lasers, Phys. Rev. Accel. Beams **19**, 020703 (2016).

[16] N. Nakamura, R. Kato, T. Miyajima, M. Shimada, T. Hotei, and R. Hajima, S2E simulation of an ERL-based high-power EUV-FEL source for lithography, J. Phys. Conf. Ser. **874**, 012013 (2017).

[17] S. Di Mitri and M. Cornacchia, Transverse emittance-preserving arc compressor for high-brightness electron beam-based light sources and colliders, Europhys. Lett. **109**, 62002 (2015).

[18] S. Di Mitri, Feasibility study of a periodic arc compressor in the presence of coherent synchrotron radiation, Nucl. Instrum. Methods Phys. Res. Sect. A **806**, 184 (2016).

[19] J. A. G. Akkermans, S. Di Mitri, D. Douglas, and I. D. Setija, Compact compressive arc and beam switchyard for energy recovery linac-driven ultraviolet free electron lasers, Phys. Rev. Accel. Beams **20**, 080705 (2017).

[20] D. Z. Khan and T. O. Raubenheimer, Novel bunch compressor chicane: The five-bend chicane, Phys. Rev. Accel. Beams **25**, 090701 (2022).

[21] C. Zhang, Y. Jiao, W. Liu, and C.-Y. Tsai, Suppression of the coherent synchrotron radiation induced emittance growth in a double-bend achromat with bunch compression, Phys. Rev. Accel. Beams **26**, 050701 (2023).

[22] F. Zeng, Y. Jiao, W. Liu, and C.-Y. Tsai, Cancelation of coherent synchrotron radiation kicks in chicane bunch compressors, Phys. Rev. Accel. Beams **28**, 070701 (2025).

[23] W. Liu, F. Zeng, and Y. Jiao, Modified coherent synchrotron radiation point-kick model with self-consistent consideration of bunch length varying, Phys. Rev. Accel. Beams **28**, 024402 (2025).

[24] C. Zhang, Y. Jiao, and C.-Y. Tsai, Quasi-isochronous triple-bend achromat with periodic stable optics and negligible coherent-synchrotron-radiation effects, Phys. Rev. Accel. Beams **24**, 060701 (2021).

[25] S. Di Mitri, M. Cornacchia, and S. Spampinati, Cancellation of coherent synchrotron radiation kicks with optics balance, Phys. Rev. Lett. **110**, 014801 (2013).

[26] Y. Jiao, X. Cui, X. Huang, and G. Xu, Generic conditions for suppressing the coherent synchrotron radiation induced emittance growth in a two-dipole achromat, Phys. Rev. ST Accel. Beams **17**, 060701 (2014).

[27] T. Hara, C. Kondo, T. Inagaki, K. Togawa, K. Fukami, S. Nakazawa, T. Hasegawa, O. Morimoto, M. Yoshioka, H. Maesaka *et al.*, High peak current operation of x-ray free-electron laser multiple beam lines by suppressing coherent synchrotron radiation effects, Phys. Rev. Accel. Beams **21**, 040701 (2018).

[28] S. Chen, H. Deng, C. Feng, R. Wang, B. Liu, and D. Wang, Design of the beam switchyard of a soft X-ray FEL user facility in Shanghai, in *Proceedings of the 9th International Particle Accelerator Conference (IPAC'18)* (JACoW Publishing, Vancouver, BC, Canada, 2018), pp. 4456–4459.

[29] J. Yan and H. Deng, Multi-beam-energy operation for the continuous-wave x-ray free electron laser, Phys. Rev. Accel. Beams **22**, 090701 (2019).

[30] X.-Y. Huang, Y. Jiao, G. Xu, and X.-H. Cui, Suppression of the emittance growth induced by coherent synchrotron radiation in triple-bend achromats, Chin. Phys. C **39**, 057001 (2015).

[31] C. Zhang, Y. Jiao, and C.-Y. Tsai, Optimization of a TBA with stable optics and minimal longitudinal dispersion and CSR-induced emittance growth, in *Proceedings of the 12th International Particle Accelerator Conference (IPAC'21)* (JACoW Publishing, Campinas, SP, Brazil, 2021), pp. 241–244.

[32] L. Wu, Z. Zhu, B. Yan, J. Yan, and H. Deng, Multi-beam-energy control unit based on triple-bend achromats, Photonics **12**, 275 (2025).

[33] M. Venturini, Design of a triple-bend isochronous achromat with minimum coherent-synchrotron-radiation-induced emittance growth, Phys. Rev. Accel. Beams **19**, 064401 (2016).

[34] R. Hajima, R-matrix analysis of the CSR effect in a future ERL light source, in *Proceedings of the 3rd Asian Particle Accelerator Conference (APAC 2004)* (Pohang Accelerator Laboratory (PAL), Gyeongju, Republic of Korea, 2004), pp. 125–127.

[35] R. Hajima, A first-order matrix approach to the analysis of electron beam emittance growth caused by coherent synchrotron radiation, Jpn. J. Appl. Phys. **42**, L974 (2003).

[36] P. Emma and R. Brinkmann, Emittance dilution through coherent energy spread generation in bending systems, in *Proceedings of the 1997 Particle Accelerator Conference* (IEEE, Vancouver, BC, Canada, 1997), Vol. 2, pp. 1679–1681.

[37] E. L. Saldin, E. A. Schneidmiller, and M. V. Yurkov, On the coherent radiation of an electron bunch moving in an arc of a circle, Nucl. Instrum. Methods Phys. Res. Sect. A **398**, 373 (1997).

[38] A. D. Brynes, P. Smorenburg, I. Akkermans, E. Allaria, L. Badano, S. Brussaard, M. Danailov, A. Demidovich, G. De Ninno, D. Gauthier *et al.*, Beyond the limits of 1D coherent synchrotron radiation, New J. Phys. **20**, 073035 (2018).

[39] D. Z. Khan and T. O. Raubenheimer, Approximated expressions for the coherent synchrotron radiation effect in various accelerator scenarios, Phys. Rev. Accel. Beams **24**, 080701 (2021).

[40] B. Liu, C.-Y. Tsai, Y. Jiao, W. Liu, F. Zeng, and W. Qin, Analytical formulas of coherent-synchrotron-radiation induced microbunching gain and emittance growth in an arbitrary achromatic four-bend chicane, Nucl. Instrum. Methods Phys. Res. Sect. A **1067**, 169703 (2024).

[41] G. Stupakov and P. Emma, CSR wake for a short magnet in ultrarelativistic limit, in *Proceedings of the 8th European Particle Accelerator Conference (EPAC 2002)* (European Physical Society Interdivisional Group on Accelerators (EPS-IGA) and CERN, Paris, France, 2002), pp. 1479–1481.

[42] D. Sagan, Bmad: A relativistic charged particle simulation library, Nucl. Instrum. Methods Phys. Res. Sect. A **558**, 356 (2006).

[43] D. Sagan, G. Hoffstaetter, C. Mayes, and U. Sae-Ueng, Extended one-dimensional method for coherent synchrotron radiation including shielding, Phys. Rev. ST Accel. Beams **12**, 040703 (2009).

[44] X.-J. Chen, S. Chen, H.-X. Deng, and D. Wang, Mitigating emittance and longitudinal profile degradation of non-ideal bunches caused by CSR in multi-bend deflecting beamlines, Nucl. Sci. Tech. **37**, 50 (2026).

[45] Y. S. Derbenev, J. Rossbach, E. L. Saldin, and V. D. Shiltsev, Microbunch radiative tail-head interaction, DESY, Hamburg, Tech. Rep. TESLA-FEL 1995-05, 1995.

[46] Y. Cai, Two-dimensional theory of coherent synchrotron radiation with transient effects, Phys. Rev. Accel. Beams **24**, 064402 (2021).

[47] R. R. Robles, J. B. Rosenzweig, and S. B. van der Geer, Three-dimensional radiative effects in the compression of ultra-short electron micro-bunches, in *Proceedings of the 12th International Particle Accelerator Conference (IPAC'21)* (JACoW Publishing, Campinas, Brazil, 2021), pp. 1577–1580.

[48] T. K. Charles, D. M. Paganin, A. Latina, M. J. Boland, and R. T. Dowd, Current-horn suppression for reduced coherent-synchrotron-radiation-induced emittance growth in strong bunch compression, Phys. Rev. Accel. Beams **20**, 030705 (2017).

[49] I. Zagorodnov and M. Dohlus, Semianalytical modeling of multistage bunch compression with collective effects, Phys. Rev. ST Accel. Beams **14**, 014403 (2011).

[50] V. Balandin, R. Brinkmann, W. Decking, and N. Golubeva, Second order achromats with arbitrary linear transfer matrices, in *Proceedings of the 2nd International Particle Accelerator Conference (IPAC'11), San Sebastián, Spain* (JACoW, San Sebastian, Spain, 2011), pp. 2160–2162.

[51] M. Borland, Simple method for particle tracking with coherent synchrotron radiation, Phys. Rev. ST Accel. Beams **4**, 070701 (2001).

[52] For sufficiently small CSR-induced emittance growth, the two cases can be approximately compared using the scaling $\Delta\epsilon_n \propto Q^2/(\sigma_z^2\gamma)$ for bunches with the same normalized longitudinal profile. The scaled emittance growths reported in Refs. [17,18] are approximately 0.19 mm mrad, while that corresponding to Ref. [19] is approximately 0.20 mm mrad; both exceed the QBA value obtained in the simulations.

[53] G. Stupakov and J. Tang, Calculation of the wake due to radiation and space charge forces in relativistic beams, Phys. Rev. Accel. Beams **24**, 020701 (2021).

[54] X. Chen, https://github.com/Chenxj62/Data-for-manuscript/tree/main/prab-78p2-pp2w (GitHub repository).